

Deep Learning for Optimal Volt/VAR Control using Distributed Energy Resources

Sarthak Gupta, *Graduate Student Member, IEEE*, Spyros Chatzivasileiadis, *Senior Member, IEEE*, and Vassilis Kekatos, *Senior Member, IEEE*

Abstract—Given their intermittency, distributed energy resources (DERs) have been commissioned with regulating voltages at fast timescales. Although the IEEE 1547 standard specifies the shape of Volt/VAR control rules, it is not clear how to optimally customize them per DER. Optimal rule design (ORD) is a challenging problem as Volt/VAR rules introduce nonlinear dynamics, require bilinear optimization models, and lurk trade-offs between stability and steady-state performance. To tackle ORD, we develop a deep neural network (DNN) that serves as a digital twin of Volt/VAR dynamics. The DNN takes grid conditions as inputs, uses rule parameters as weights, and computes equilibrium voltages as outputs. Thanks to this genuine design, ORD is reformulated as a deep learning task using grid scenarios as training data and aiming at driving the predicted variables being the equilibrium voltages close to unity. The learning task is solved by modifying efficient deep-learning routines to enforce constraints on rule parameters. In the course of DNN-based ORD, we also review and expand on stability conditions and convergence rates for Volt/VAR rules on single-/multi-phase feeders. To benchmark the optimality and runtime of DNN-based ORD, we also devise a novel mixed-integer nonlinear program formulation. Numerical tests showcase the merits of DNN-based ORD.

Index Terms—IEEE 1547.8 Standard, linearized distribution flow model, multiphase feeders, gradient backpropagation.

I. INTRODUCTION

DERs such as solar photovoltaics, are being advocated as a means to battle climate change, shave peak demand, and improve reliability. Despite the obvious benefits, voltage fluctuations arising from uncertainties in DERs may hinder their large-scale adoption. Fortunately, optimal control strategies for inverter-interfaced DERs to provide voltage regulation can alleviate the previous concern. Under centralized voltage regulation, a supervisory entity consolidates load and generation measurements across the grid and solves an optimal power flow (OPF) to determine setpoints for DERs [1]–[3]. Albeit easier to conceive, centralized schemes suffer from considerable communication and computational overhead and privacy issues, and presume a detailed feeder model is available.

On the other hand, *local* voltage regulation schemes for DERs entail calculating control setpoints solely on the basis of data locally accessible by the DERs, such as load, solar generation, and voltage measurements at the grid interface. The IEEE 1547.8 Standard prescribes a local control scheme whereby DER setpoints are produced by *control rules* taking the form of piecewise linear functions of local measurements [4]. Local rules however are known to produce sub-optimal setpoints [5], [6]. Nevertheless, autonomy and simplicity are lucrative features of local schemes for real-time DER control. Focusing on

Volt/VAR control, this work delves into the study and optimal design of local rules.

Volt/VAR rules compute reactive power setpoints for inverters based on the local deviation from the nominal voltage. Since voltages are affected by reactive setpoints, Volt/VAR rules give rise to closed-loop dynamics, which can become unstable under steep control rule slopes [7]–[9]. While the aforementioned works study the convergence and stability of Volt/VAR control rules, they do not address how to design such rules, i.e., select their exact shape, in the first place. Prior efforts on designing DER rules either resort to heuristics [10]–[12], deal with non-dynamic Watt/VAR rules [13], or restrict themselves to affine Volt/VAR rules [14], [15]. Different from above, our recent work in [16] formulates a bilevel optimization to design the slopes, deadband, saturation, and reference voltages for the Volt/VAR rules as prescribed by the IEEE 1547.8 Standard. The bilevel optimization considers a number of possible grid scenarios, and upon leveraging the properties of the system at equilibrium, it finds stationary points using projected gradient descent iterates.

Our present work extends [16], and improves upon the previously cited literature in four directions: *c1*) Most of the existing works focus on simplified single-phase models of distribution feeders and do not capture inter-phase coupling. We extend the analysis in [9] to provide a polytopic restriction on the slope of control curves, which guarantees the stability of Volt/VAR rules per the IEEE 1547 Standard to multiphase feeders; *c2*) We design a digital twin of Volt/VAR dynamics using a DNN. The digital twin accepts grid conditions as the input, the control rule parameters as weights, and computes approximate equilibrium voltages at its output. Based on the rate of convergence of Volt/VAR dynamics, we determine the minimum depth for the DNNs to simulate such dynamics up to the desired level of accuracy; *c3*) We cast the problem of optimal design of Volt/VAR rules as training the DNN-based digital twin. The training process involves stochastic projected gradient updates (SPGD) that leverage efficient, off-the-shelf Python libraries to train the DNNs; *c4*) Exploiting the bilevel structure, we also formulate ORD as a novel mixed-integer nonlinear program (MINLP). Although the MINLP-based approach does not scale well with the number of DERs and grid scenarios, it serves as a benchmark for the optimality and computational speed of DNN-based ORD.

We next expound upon how our work differs from prior works utilizing machine learning for smart inverter control. DNNs have been extensively employed before for optimal DER control under OPF formulations, with the objective of minimizing energy losses and energy costs; see e.g., [17]–

[20]. Support vector machines and Gaussian processes have also been suggested for reactive power control using smart inverters [21], [22]. However, none of the above references aim at modeling the IEEE 1547-type piecewise linear, local, Volt/VAR rules. Furthermore, the existing problem formulations preclude the presence of closed-loop dynamics and are not nuanced by stability concerns as in the present work. In terms of using a DNN to model piecewise linear Volt/VAR control rules, our work bears some similarities with [23]. Reference [23] models piecewise linear control rules, using a NN with a single hidden layer. However, the DNN-based approach is not extended to capture Volt/VAR dynamics end-to-end and model equilibrium voltages, primarily because its focus is on optimal control of transient dynamics. In contrast, the aim of the present work is to design control rules that produce equilibrium voltages close to unity across many scenarios. Moreover, reference [23] does not discuss other topics covered in this work such as the IEEE 1547-type Volt/VAR rules, their convergence speed, and the implications of Volt/VAR control in multiphase feeders.

This paper is organized as follows. Section II presents the feeder model. Section III discusses the equilibrium and convergence of Volt/VAR rules on single-phase feeders. Section IV casts the problem of ORD in single-phase feeders as a deep learning task. Section V formulates the benchmark MINLP that also solves ORD for single-phase feeders. Section VI extends DNN-based ORD to multiphase feeders, while providing the necessary stability and convergence claims. Section VII presents numerical tests confirming the efficacy of the proposed DNN-based ORD on single- and multi-phase feeders. Conclusions and future directions are drawn in Section VIII.

II. FEEDER MODELING PRELIMINARIES

Consider a feeder rooted at the substation. Although the feeder can be single-phase or multiphase, it features a tree structure in terms of buses. For multiphase feeders, a bus may be serving one to three phases; a valid pair of bus and phase will be referred to as a *node*. For single-phase feeders, the terms *bus* and *node* will be used interchangeably. The substation is indexed by 0 and is considered balanced; all remaining nodes are indexed by $n \in \mathcal{N} := \{1, \dots, N\}$. All DERs are assumed to be single-phase and be able to provide reactive power control. For simplicity, each node is assumed to host a DER; we briefly discuss the minor modifications to deal with the more practical setting where not all nodes host DERs. Our numerical tests evaluate the latter setting.

To study the effect of power injections on voltage magnitudes, we use an approximate linearized grid model. Let the active/reactive power injections and voltage magnitudes (henceforth simply voltages) at the non-substation nodes be collected into the N -length vectors \mathbf{p} , \mathbf{q} , and \mathbf{v} , respectively. The linearized grid model relates these quantities as [24]

$$\mathbf{v} \simeq \mathbf{R}\mathbf{p} + \mathbf{X}\mathbf{q} + v_0\mathbf{1} \quad (1)$$

where v_0 is the substation voltage, and real-valued matrices \mathbf{R} and \mathbf{X} depend on line impedances and feeder topology.

If \mathbf{p}^g and \mathbf{p}^ℓ denote the active power generated by DERs and that consumed by the loads accordingly, then $\mathbf{p} = \mathbf{p}^g -$

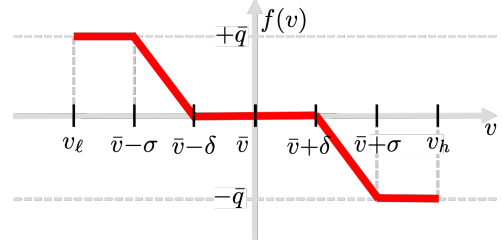


Fig. 1. The piecewise linear Volt/VAR control rule $f(v)$ provisioned by the IEEE 1547 standard [4]. The x -axis corresponds to the local voltage magnitude and the y -axis to the inverter setpoint for reactive power injection.

\mathbf{p}^ℓ . Reactive power injections can be decomposed similarly as $\mathbf{q} = \mathbf{q}^g - \mathbf{q}^\ell$. Supposing \mathbf{p} and \mathbf{q}^ℓ are uncontrolled and vary with time, reactive power compensation entails adjusting \mathbf{q}^g to maintain \mathbf{v} around one per unit (pu). To isolate the effect of DER reactive injections on voltages, rearrange (1) as

$$\mathbf{v} = \mathbf{X}\mathbf{q}^g + \tilde{\mathbf{v}} = \mathbf{X}\mathbf{q} + \tilde{\mathbf{v}} \quad (2)$$

where the notation is slightly abused by denoting \mathbf{q}^g as \mathbf{q} for simplicity. The uncontrolled quantities are captured in vector $\tilde{\mathbf{v}} := \mathbf{R}(\mathbf{p}^g - \mathbf{p}^\ell) - \mathbf{X}\mathbf{q}^\ell + v_0\mathbf{1}$, where $\tilde{\mathbf{v}}$ models voltages had it not been for reactive power compensation. Vector $\tilde{\mathbf{v}}$ will be henceforth termed the vector of *grid conditions*.

Given its importance in Volt/VAR control, let us summarize some properties of the sensitivity matrix \mathbf{X} appearing in (2). For single-phase feeders, matrix \mathbf{X} is known to be symmetric, positive definite, and with positive entries; see e.g., [25], [26]. For multiphase feeders however, matrix \mathbf{X} is non-symmetric and has positive as well as negative entries [27]. Nonetheless, under conditions typically met in practice [27], matrix \mathbf{X} remains positive definite for multiphase feeders in the sense $\mathbf{z}^\top \mathbf{X} \mathbf{z} > 0$ for all $\mathbf{z} \neq \mathbf{0}$. These nuances of \mathbf{X} call for relatively different treatments of Volt/VAR control between single- (Sections III–IV) and multi-phase feeders (Section VI).

III. CONTROL RULES FOR SINGLE-PHASE FEEDERS

The IEEE 1547.8 standard provisions four modes of reactive power control [4]: constant power, constant power factor, Watt/VAR, and Volt/VAR. We focus on the last one as being the most grid-adaptive. This mode enables the inverters to respond to local voltage deviations via a piecewise linear control curve $f(v)$, like the one depicted in Fig. 1. The curve consists of a deadband of length 2δ centered around \bar{v} ; two affine regions; and two regions wherein reactive injections saturate at $\pm\bar{q}$. The standard constraints curve parameters as

$$0.95 \leq \bar{v} \leq 1.05 \quad (3a)$$

$$0 \leq \delta \leq 0.03 \quad (3b)$$

$$\delta + 0.02 \leq \sigma \leq 0.18 \quad (3c)$$

$$0 \leq \bar{q} \leq \hat{q} \quad (3d)$$

Per (3d), the saturation value \bar{q} can be equal to the reactive power capability \hat{q} of the inverter, but also smaller than that.

The rule of Fig. 1 is parameterized by $(\bar{v}, \delta, \sigma, \bar{q})$, which can be customized per bus n as $(\bar{v}_n, \delta_n, \sigma_n, \bar{q}_n)$. The rule can

be alternatively parameterized by $(\bar{v}_n, \alpha_n, \delta_n, \bar{q}_n)$, where α_n is the negative slope of the affine segment and is defined as

$$\alpha_n = \frac{\bar{q}_n}{\sigma_n - \delta_n} > 0. \quad (4)$$

Let vectors $(\bar{\mathbf{v}}, \boldsymbol{\alpha}, \boldsymbol{\delta}, \bar{\mathbf{q}})$ collect $(\bar{v}_n, \alpha_n, \delta_n, \bar{q}_n)$ for all $n \in \mathcal{N}$; and stack such vectors together in vector $\mathbf{z} := (\bar{\mathbf{v}}, \boldsymbol{\alpha}, \boldsymbol{\delta}, \bar{\mathbf{q}})$.

The interaction of Volt/VAR-controlled DERs with the grid results in the non-linear discrete-time dynamics

$$\mathbf{v}^t = \mathbf{X}\mathbf{q}^t + \bar{\mathbf{v}} \quad (5a)$$

$$\mathbf{q}^{t+1} = \mathbf{f}_{\mathbf{z}}(\mathbf{v}^t) \quad (5b)$$

where vector function $\mathbf{f}_{\mathbf{z}}(\mathbf{v}^t)$ represents the action of Volt/VAR rules across all nodes and is parameterized by \mathbf{z} . If stable, the dynamics in (5) enjoy an equilibrium under any grid condition $\tilde{\mathbf{v}}$ [26]. In fact, the inverter setpoints at equilibrium coincide with the unique minimizer of the convex program [26]

$$\mathbf{q}^*(\mathbf{z}, \tilde{\mathbf{v}}) = \arg \min_{-\bar{\mathbf{q}} \leq \mathbf{q}} F(\mathbf{q}) := V(\mathbf{q}) + C(\mathbf{q}). \quad (6)$$

The two components of the objective $F(\mathbf{q})$ are defined as

$$V(\mathbf{q}) := \frac{1}{2} \mathbf{q}^\top \mathbf{X} \mathbf{q} + \mathbf{q}^\top (\tilde{\mathbf{v}} - \bar{\mathbf{v}}) \quad (7a)$$

$$C(\mathbf{q}) := \sum_{n \in \mathcal{N}} \left(\frac{1}{2\alpha_n} q_n^2 + \delta_n |q_n| \right). \quad (7b)$$

Component $V(\mathbf{q})$ can be equivalently expressed as [26]

$$V(\mathbf{q}) = \frac{1}{2} (\mathbf{v} - \bar{\mathbf{v}})^\top \mathbf{X}^{-1} (\mathbf{v} - \bar{\mathbf{v}}) + \text{constants}. \quad (8)$$

Because $\mathbf{X} \succ 0$, function $V(\mathbf{q})$ is an ℓ_2 -norm of $(\mathbf{v} - \bar{\mathbf{v}})$. Hence, minimizing $V(\mathbf{q})$ aims at bringing voltages close to reference voltages. Nonetheless, problem (7) involves also $C(\mathbf{q})$ in its cost. Based on (6) and to best regulate voltages, one would try setting $\boldsymbol{\alpha}$ to infinity and $\boldsymbol{\delta}$ to zero so $C(\mathbf{q}) = 0$ and the equilibrium setpoints minimize only $V(\mathbf{q})$. This course of action has a dynamic stability implication as detailed next.

Reference [9] guarantees that Volt/VAR dynamics are stable if $\|\text{dg}(\boldsymbol{\alpha})\mathbf{X}\|_2 < 1$, where $\text{dg}(\boldsymbol{\alpha})$ is a diagonal matrix having $\boldsymbol{\alpha}$ on its diagonal. To be satisfied as a strict inequality, the condition can be strengthened as $\|\text{dg}(\boldsymbol{\alpha})\mathbf{X}\|_2 \leq 1 - \epsilon$ for some $\epsilon \in (0, 1)$.

Definition 1. Volt/VAR rules satisfying $\|\text{dg}(\boldsymbol{\alpha})\mathbf{X}\|_2 \leq 1 - \epsilon$ for $\epsilon \in (0, 1)$ will be henceforth termed ϵ -stable.

To avoid the spectral norm condition $\|\text{dg}(\boldsymbol{\alpha})\mathbf{X}\|_2 \leq 1 - \epsilon$, we have previously proposed a polytopic restriction [16]:

$$\mathbf{X}\boldsymbol{\alpha} \leq (1 - \epsilon)\mathbf{1} \quad (9a)$$

$$\alpha_n \leq \frac{1 - \epsilon}{\sum_{m \in \mathcal{N}} X_{nm}}, \quad \forall n \in \mathcal{N}. \quad (9b)$$

The next section develops methods for selecting the Volt/VAR rule parameters \mathbf{z} so that a voltage regulation objective is minimized for a set of grid scenarios. For single-phase feeders, Section IV reformulates (ORD) as the problem of training a neural network, while Section V tackles ORD as a mixed-integer nonlinear program. For multiphase feeders, solving ORD is dealt with in Section VI.

IV. ORD FOR 1ϕ FEEDERS VIA DEEP LEARNING

Because Volt/VAR rules are used so inverters can operate autonomously, it is reasonable to assume that rule parameters \mathbf{z} are updated infrequently, say every 2 hours. Then, rules \mathbf{z} should be optimized while considering the possibly diverse loading conditions the feeder may experience over those 2 hours. To account for such conditions, suppose we are given a set of S load/solar scenarios $\{(\mathbf{p}_s^g, \mathbf{p}_s^\ell, \mathbf{q}_s^\ell)\}_{s=1}^S$. Each scenario is related to grid condition vector [see (1)]

$$\tilde{\mathbf{v}}_s := \mathbf{R}(\mathbf{p}_s^g - \mathbf{p}_s^\ell) - \mathbf{X}\mathbf{q}_s^\ell.$$

Let $\mathbf{q}^*(\mathbf{z}, \tilde{\mathbf{v}}_s)$ or simply $\mathbf{q}_s^*(\mathbf{z})$ denote the equilibrium setpoints reached by stable Volt/VAR rules parameterized by \mathbf{z} under grid conditions $\tilde{\mathbf{v}}_s$. Unfortunately, setpoints $\mathbf{q}_s^*(\mathbf{z})$ cannot be expressed as in closed form. They can be computed by either iterating (5), or as the minimizer of (6). The related equilibrium voltage is $\mathbf{v}_s^*(\mathbf{z}) := \mathbf{X}\mathbf{q}_s^*(\mathbf{z}) + \tilde{\mathbf{v}}_s$ from (1).

We pose the ORD task as a minimization problem over \mathbf{z} :

$$\begin{aligned} \min_{\mathbf{z}} \quad & \frac{1}{2S} \sum_{s=1}^S \|\mathbf{X}\mathbf{q}_s^*(\mathbf{z}) + \tilde{\mathbf{v}}_s - \mathbf{1}\|_2^2 \\ \text{s.to} \quad & (3), (9) \end{aligned} \quad (10)$$

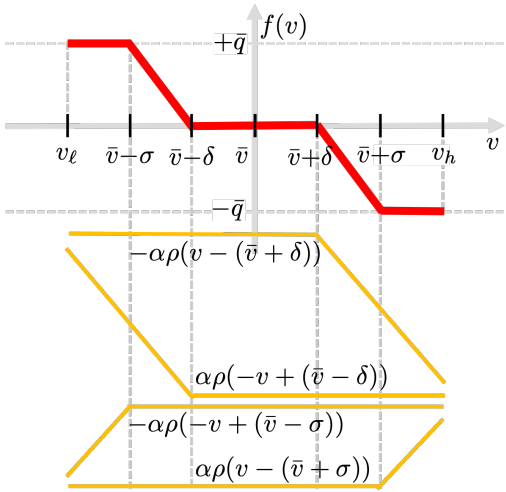
to minimize the Euclidean distance of equilibrium voltages from unity, averaged across scenarios. Constraints (3) and (9) ensure rules are stable and compliant with the IEEE 1547.

One may wonder why are we not satisfied with the fact that any stable rule \mathbf{z} settles at the minimizer of (6), which is seemingly a meaningful equilibrium. Such equilibrium may be insufficient due to three reasons: *i*) The term $V(\mathbf{q})$ is a rotated ℓ_2 -norm of $(\mathbf{v} - \bar{\mathbf{v}})$, so that voltage deviations are weighted unequally across buses; *ii*) If DERs are sited only on a subset $\mathcal{G} \subset \mathcal{N}$ of nodes, the cost $V(\mathbf{q})$ gets modified as $V_{\mathcal{G}}(\mathbf{q}_{\mathcal{G}}) = \frac{1}{2} (\mathbf{v}_{\mathcal{G}} - \bar{\mathbf{v}}_{\mathcal{G}})^\top \mathbf{X}_{\mathcal{G}}^{-1} (\mathbf{v}_{\mathcal{G}} - \bar{\mathbf{v}}_{\mathcal{G}})$, where subscript \mathcal{G} denotes the subvectors/submatrix obtained by keeping the rows/columns corresponding to \mathcal{G} ; see [16]. Such cost may not be representative of $\|\mathbf{v} - \bar{\mathbf{v}}\|_2^2$; and *iii*) As discussed earlier, stability limitations do not allow us to set $\boldsymbol{\alpha}$ to infinity although it seems desirable from a voltage regulation standpoint. The aforesaid reasons motivate the need to optimally design \mathbf{z} so the induced equilibrium voltages $\mathbf{v}_s^*(\mathbf{z})$ are better regulated.

Albeit simply stated, problem (10) is computationally challenging as $\mathbf{q}_s^*(\mathbf{z})$ is the solution of the *inner* minimization problem (6), which is parameterized by \mathbf{z} . Thereby, the ORD task is a *bilevel optimization* over \mathbf{z} : The *outer* problem (10) depends on S inner problems of the form (6), one per scenario.

Our first strategy towards tackling (10) is to replace the inner problem with a DNN that simulates the Volt/VAR dynamics. This DNN has \mathbf{z} as weights, accepts $\tilde{\mathbf{v}}_s$ as input, and outputs the equilibrium voltages $\mathbf{v}_s^*(\mathbf{z})$. Let the DNN output be denoted by $\Phi(\tilde{\mathbf{v}}_s; \mathbf{z})$. The key idea is that if $\Phi(\tilde{\mathbf{v}}_s; \mathbf{z})$ are the equilibrium voltages for rule \mathbf{z} over scenario s , then problem (10) becomes the supervised training task:

$$\begin{aligned} \min_{\mathbf{z}} \quad & L(\mathbf{z}) := \frac{1}{2S} \sum_{s=1}^S \|\Phi(\tilde{\mathbf{v}}_s; \mathbf{z}) - \mathbf{1}\|_2^2 \\ \text{s.to} \quad & (3), (9). \end{aligned} \quad (11)$$

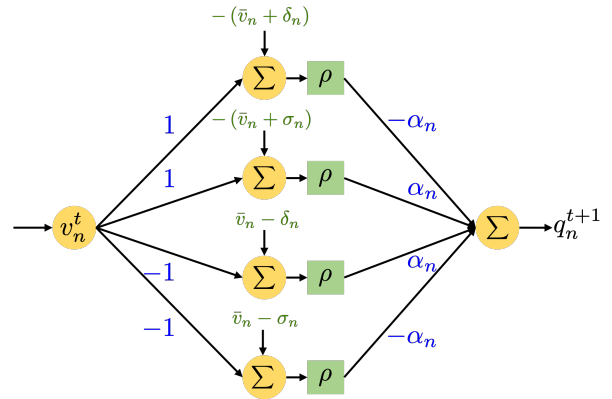
Fig. 2. Volt/VAR rule $f(v)$ expressed as a sum of ReLUs.

To draw a useful analogy, scenarios $\tilde{\mathbf{v}}_s$ are analogous to feature vectors in regression problems; equilibrium voltages $\mathbf{v}_s^* = \Phi(\tilde{\mathbf{v}}_s; \mathbf{z})$ are the predictions for feature vectors; and $\mathbf{1}$ is the (constant) target label for the prediction. Formulating (10) as (11) allows us to leverage efficient DNN libraries for optimizing \mathbf{z} . With this motivation in mind, we next design the DNN, and then describe the steps to train it.

A. Designing a Digital Twin of Volt/VAR Dynamics

The Volt/VAR curve of Fig. 1 can be interpreted as a superposition of four piecewise-linear functions, each with a single breakpoint, as shown in Fig. 2. These functions can be thought of as the outputs of rectified linear units (ReLU) $\rho(x)$, which return x for $x > 0$; and 0 otherwise. To get the different breakpoints and slopes as in Figure 2, the ReLU units need the appropriate inputs and scaling. The required mathematical operations can be implemented through the DNN of Fig. 3, which takes v_n^t as input and computes the setpoint q_n^{t+1} at its output. The input and output layers have one neuron each. The hidden layer consists of four neurons. The weights of the hidden layer are fixed to $[1, 1, -1, -1]^\top$, but its bias vector is trainable and given by $[-(\bar{v} + \delta), -(\bar{v} + \sigma), \bar{v} - \delta, \bar{v} - \sigma]^\top$. Each of the four neurons in the hidden layer is equipped with a ReLU unit. The output layer has a trainable weight vector $[-\alpha, \alpha, \alpha, -\alpha]^\top$ and the bias is fixed at 0.

Heed that the NN of Fig. 3 implements the Volt/VAR curve for a single inverter and a single time step as $q_n^{t+1} = f_n(v_n^t)$. To simulate the entire Volt/VAR network dynamics of (5), we will treat the NN of Fig. 3 as a building block and replicate it across inverters and time. Let VC_n represent the NN module running one time step for inverter n . This module is parameterized by $(\bar{v}_n, \alpha_n, \sigma_n, \delta_n)$. With a slight abuse of terminology, let the collection of VC_n 's for all inverters be labeled as a single *layer*. These modules are stacked vertically as shown in Fig. 4. Each one of these layers implements (5b) by receiving \mathbf{v}^t as input, and producing setpoints \mathbf{q}^{t+1} as outputs for a single time t . The setpoints \mathbf{q}^{t+1} in turn produce voltages $\mathbf{v}^{t+1} = \mathbf{X}\mathbf{q}^{t+1} + \tilde{\mathbf{v}}$ per the grid model (5a). To

Fig. 3. Volt/VAR rule $f(v)$ model using a DNN with 1 hidden layer.

simulate the dynamics over time, the new voltages \mathbf{v}^{t+1} are passed to the next layer, and the process is repeated for T steps. Structurally, these interactions result in a larger DNN with T repeating layers, one layer per iteration of (5), as shown in Figure 4. The simulation of dynamics over T iterations is then simply equivalent to performing a forward pass through the larger DNN with $\tilde{\mathbf{v}}$ as the input. To implement (5a), the input $\tilde{\mathbf{v}}$ (grid scenario vector) is also propagated to the inner layers via so termed *skip connections*.

It is worth stressing that each module VC_n is replicated horizontally across the T times. This implies significant *weight sharing* across the T layers. Therefore, the number of trainable parameters $\hat{\mathbf{z}} := (\bar{\mathbf{v}}, \alpha, \delta, \sigma)$ remains fixed at $4N$, irrespective of the DNN depth T . This weight-sharing aspect results in computational and memory-related efficiencies for DNN storing, prediction, and training, and has been instrumental in the success of architectures such as recurrent (RNN), convolutional (CNN), or graph (GNN) neural networks. In fact, it is possible to obtain a recurrent ‘rolled’ representation of the larger DNN of Fig. 4, as shown in Fig. 5, allowing one to utilize RNN-specific functionalities in DNN libraries.

In a nutshell, the DNN of Fig. 4 simulates Volt/VAR dynamics across T times. In other words, once fed with a grid condition vector $\tilde{\mathbf{v}}_s$, its output will approximate the equilibrium voltages \mathbf{v}_s^* reached by Volt/VAR dynamics under rule \mathbf{z} . As a result, optimizing over \mathbf{z} by training the DNN so that equilibrium voltages $\{\mathbf{v}_s^*(\mathbf{z})\}_{s=1}^S$ come close to one pu, serves the purposes of ORD. Surrogating Volt/VAR dynamics by the DNN is effective only if the DNN depth T is sufficiently large. *How deep should the DNN be so that its output $\Phi(\tilde{\mathbf{v}}_s; \hat{\mathbf{z}})$ is close to \mathbf{v}_s^* ?* Because a DNN of depth T simulates exactly the Volt/VAR dynamics up to time T , the answer for selecting T is apparently the settling time of the Volt/VAR dynamics as detailed next and shown in the appendix.

Proposition 1. Suppose ϵ -stable Volt/VAR rules are described by \mathbf{z} . The depth T of the DNN in Fig. 4 required to ensure $\|\Phi(\tilde{\mathbf{v}}; \mathbf{z}) - \mathbf{v}^*(\mathbf{z})\|_2 \leq \epsilon_1$ for all grid conditions $\tilde{\mathbf{v}}$ is

$$T \geq \frac{\log \frac{2\|\mathbf{X}\|_2\|\mathbf{q}\|_2}{\epsilon_1}}{\log(1 - \epsilon)^{-1}}.$$

The result implies that the minimum depth T grows log-

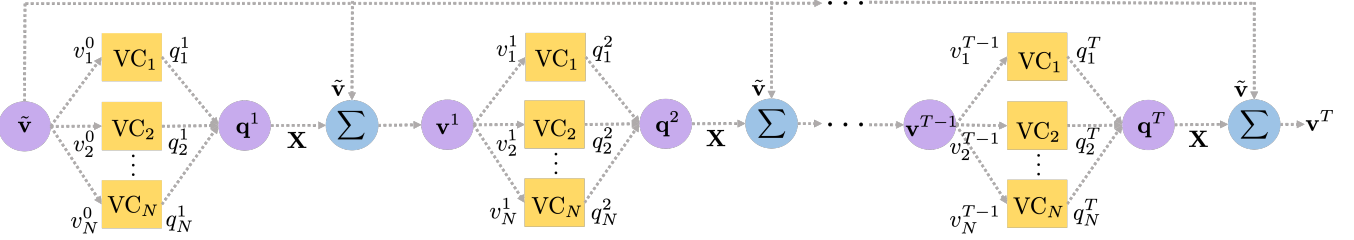


Fig. 4. DNN-based digital twin for the Volt/VAR dynamics of (5). The DNN is structured so that T time steps are arranged horizontally. The modules VC_n 's implementing the Volt/VAR curves for each one of the N inverters are stacked vertically. Skip connections propagate the input vector (grid scenario) $\tilde{\mathbf{v}}$ to each time instant to implement $\mathbf{v}^{t+1} = \mathbf{X}\mathbf{q}^{t+1} + \tilde{\mathbf{v}}$.

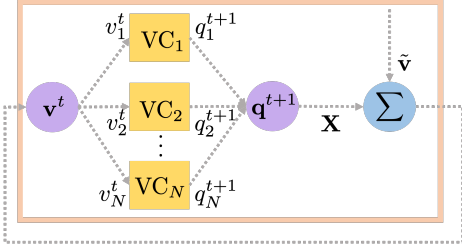


Fig. 5. Recurrent representation (RNN) of the digital twin of Fig. 4.

arithmically with the desired accuracy ϵ_1 and the stability margin ϵ . Plugging in the typical values $\epsilon_1 = 10^{-4}$, $\|\mathbf{X}\|_2 = 4.63 \cdot 10^{-1}$ for IEEE 37-bus feeder, $\|\dot{\mathbf{q}}\|_2 = 0.1$, and $\epsilon = 0.3$, the bound yields a comfortably small number of $T \geq 20$ layers. For $\epsilon_1 = 10^{-6}$, the number of layers T increases to 32, demonstrating the scalability of the approach.

B. DNN Training

With rule parameters $\hat{\mathbf{z}}$ embedded as DNN weights and biases, the optimal Volt/VAR curves are obtained by training $\Phi(\tilde{\mathbf{v}}_s; \hat{\mathbf{z}})$. Conventional DNN training uses stochastic gradient descent (SGD) to update the DNN parameters and eventually minimize the *loss function* in (11). However, parameters $\hat{\mathbf{z}}$ should satisfy constraints (3) and (9). Plain SGD may fail to return a feasible \mathbf{z} . This can be circumvented by using projected stochastic gradient (PSGD) updates. PSGD updates first compute an intermediate quantity $\hat{\mathbf{x}}^{i+1}$ via gradient descent

$$\hat{\mathbf{x}}^{i+1} = \hat{\mathbf{z}}^i - \frac{\mu}{2B} \nabla_{\hat{\mathbf{z}}^i} \left(\sum_{s \in \mathcal{B}_i} \|\Phi(\tilde{\mathbf{v}}_s; \hat{\mathbf{z}}) - \mathbf{1}\|_2^2 \right) \quad (12)$$

where $\mu > 0$ is the step size; set \mathcal{B}_i is a batch of B scenarios (a subset of the original S scenarios); and $\nabla_{\hat{\mathbf{z}}^i}(\cdot)$ is the gradient of the loss function with respect to $\hat{\mathbf{z}}$ evaluated at $\hat{\mathbf{z}} = \hat{\mathbf{z}}^i$. The gradient term in (12) is calculated efficiently thanks to *gradient back-propagation*.

The second step for PSGD updates entails projecting $\hat{\mathbf{x}}^{i+1}$ into the feasible space defined by (3) and (9). To this end, we first transform $\hat{\mathbf{x}}^{i+1}$ from parameter space $(\tilde{\mathbf{v}}, \mathbf{c}, \boldsymbol{\delta}, \boldsymbol{\sigma})$ to space $(\tilde{\mathbf{v}}, \mathbf{c}, \boldsymbol{\delta}, \boldsymbol{\sigma})$, where vector \mathbf{c} has entries $c_n := 1/\alpha_n$. Variable $\hat{\mathbf{x}}^{i+1}$ transformed in the new space is called $\tilde{\mathbf{x}}^{i+1}$. The transformation is a one-to-one mapping between the two spaces, and is used so that the feasibility set induced by (3) and (9) is convex, and so it is easy to project onto it. We

proposed this transformation in [16]. We review it here for completeness. Using (4), constraint (3d) is expressed as

$$0 \leq \boldsymbol{\sigma} - \boldsymbol{\delta} \leq \mathbf{c} \odot \dot{\mathbf{q}} \quad (13)$$

where \odot means element-wise multiplication. Constraints (9) can be expressed in terms of \mathbf{c} instead of $\boldsymbol{\alpha}$ as [16]

$$\mathbf{c} \geq \frac{1}{1-\epsilon} \mathbf{X} \mathbf{1} \quad (14a)$$

$$\mathbf{X} \mathbf{a} \leq (1-\epsilon) \cdot \mathbf{1} \quad (14b)$$

$$\mathbf{a} \odot \mathbf{c} \geq \mathbf{1}, \quad \forall n \in \mathcal{N} \quad (14c)$$

where \mathbf{a} is an auxiliary variable. Constraint (14c) can be rewritten as a second-order cone. In [16], we show how (14) is equivalent to (9). The quantity $\tilde{\mathbf{x}}^{i+1}$ can now be projected onto the feasible space via the convex minimization

$$\begin{aligned} \tilde{\mathbf{x}}^{i+1} &= \arg \min_{\mathbf{z}} \|\tilde{\mathbf{x}}^{i+1} - \mathbf{z}\|_2^2 \\ \text{s.to } & (3a) - (3c), (13), (14). \end{aligned} \quad (15)$$

The PSGD update is completed by transforming $\tilde{\mathbf{x}}^{i+1}$ from space $(\tilde{\mathbf{v}}, \mathbf{c}, \boldsymbol{\delta}, \boldsymbol{\sigma})$ back to space $(\tilde{\mathbf{v}}, \boldsymbol{\alpha}, \boldsymbol{\delta}, \boldsymbol{\sigma})$ to get $\hat{\mathbf{z}}^{i+1}$.

The proposed DNN training can be implemented in Python using DNN libraries such as PyTorch [28]. Step (12) is the standard SGD update pertaining to the loss function of (11) over the batch of training labels $\{\tilde{\mathbf{v}}_s, 1\}_{\mathcal{B}_i}$. As with standard DNN training, adaptive moment-based algorithms such as Adam can be used to enable fast convergence and avoid saddle points. The DNN weights and biases are transformed between the parameter spaces, and then passed to a convex optimization module to implement the projection step of (15). In the last step, DNN weights and biases are updated with the new projected parameters, upon transformation to the original space. The steps are repeated for several epochs.

V. ORD FOR 1ϕ FEEDERS AS AN MINLP

A second approach towards solving the bilevel program in (10) is to replace each inner problem by its first-order optimality conditions and append these conditions as constraints to the outer problem. To capture complementary slackness, we will introduce binary variables and use the so-termed big-M trick to eventually express the outer problem as a mixed-integer nonlinear program (MINLP). The process is delineated next. Although this MINLP approach does not scale gracefully with the number of DERs and/or scenarios, it serves as a benchmark for the DNN-based ORD.

We first transform (6) to a differentiable form as

$$\min_{\mathbf{q}, \mathbf{w}} \frac{1}{2} \mathbf{q}^\top (\mathbf{X} + \text{dg}(\mathbf{c})) \mathbf{q} + \mathbf{q}^\top (\tilde{\mathbf{v}}_s - \bar{\mathbf{v}}) + \boldsymbol{\delta}^\top \mathbf{w} \quad (16a)$$

$$\text{s.to } -\mathbf{w} \leq \mathbf{q} \leq \mathbf{w} : \quad (\underline{\boldsymbol{\lambda}}, \bar{\boldsymbol{\lambda}}) \quad (16b)$$

$$-\bar{\mathbf{q}} \leq \mathbf{q} \leq \bar{\mathbf{q}} : \quad (\underline{\boldsymbol{\mu}}, \bar{\boldsymbol{\mu}}) \quad (16c)$$

where vector \mathbf{c} has entries $c_n := 1/\alpha_n$, and variable \mathbf{w} has been introduced to deal with the non-differentiable terms $|q_n|$ in (6). Slightly abusing notation, denote the optimal primal/dual variables of (16) by $(\mathbf{q}, \mathbf{w}; \underline{\boldsymbol{\lambda}}, \bar{\boldsymbol{\lambda}}, \underline{\boldsymbol{\mu}}, \bar{\boldsymbol{\mu}})$. Although the variables vary per scenario, we suppress subscript s for simplicity. These variables satisfy the optimality conditions

$$(\mathbf{X} + \text{dg}(\mathbf{c})) \mathbf{q} + \tilde{\mathbf{v}}_s - \bar{\mathbf{v}} - \underline{\boldsymbol{\lambda}} + \bar{\boldsymbol{\lambda}} - \underline{\boldsymbol{\mu}} + \bar{\boldsymbol{\mu}} = \mathbf{0} \quad (17a)$$

$$\boldsymbol{\delta} - \underline{\boldsymbol{\lambda}} - \bar{\boldsymbol{\lambda}} = \mathbf{0} \quad (17b)$$

$$-\mathbf{w} \leq \mathbf{q} \leq \mathbf{w} \quad (17c)$$

$$-\bar{\mathbf{q}} \leq \mathbf{q} \leq \bar{\mathbf{q}} \quad (17d)$$

$$\underline{\boldsymbol{\lambda}}, \bar{\boldsymbol{\lambda}}, \underline{\boldsymbol{\mu}}, \bar{\boldsymbol{\mu}} \geq \mathbf{0} \quad (17e)$$

$$\bar{\boldsymbol{\lambda}} \odot (\mathbf{q} - \mathbf{w}) = \mathbf{0} \quad (17f)$$

$$\underline{\boldsymbol{\lambda}} \odot (-\mathbf{q} - \mathbf{w}) = \mathbf{0} \quad (17g)$$

$$\bar{\boldsymbol{\mu}} \odot (\mathbf{q} - \bar{\mathbf{q}}) = \mathbf{0} \quad (17h)$$

$$\underline{\boldsymbol{\mu}} \odot (-\mathbf{q} - \bar{\mathbf{q}}) = \mathbf{0}. \quad (17i)$$

Equalities (17a)–(17b) follow from Lagrangian optimality; and inequalities (17c)–(17e) from primal/dual feasibility. Inequalities (17f)–(17i) are complementary slackness conditions.

The bilevel problem in (10) can be now reduced to a single-level formulation upon appending conditions (17) as constraints to (10) per scenario s . Such constraints essentially ensure that $\mathbf{q}_s^*(\mathbf{z})$ is indeed the minimizer of (6). Nonetheless, constraint (17a) and the complementary conditions introduce bilinear terms. Bilinearity can be partially addressed by handling complementary slackness conditions through the big-M trick. For example, condition (17f) can be expressed as

$$\mathbf{0} \leq \bar{\boldsymbol{\lambda}} \leq M_1 \mathbf{b} \quad (18a)$$

$$\mathbf{0} \leq \mathbf{q} - \mathbf{w} \leq M_2 (1 - \mathbf{b}) \quad (18b)$$

where \mathbf{b} is an N -dimensional binary variable, and (M_1, M_2) are large positive constants. The latter can be selected as $M_2 = 2\bar{\mathbf{q}}$, while the former can be set to a numerically estimated upper bound of the corresponding dual variables $\underline{\boldsymbol{\lambda}}$.

Since (17)–(18) contain \mathbf{c} and $\bar{\mathbf{q}}$, the constraints (3) and (9) need to be rewritten in terms of \mathbf{c} and $\bar{\mathbf{q}}$ as well. To this end, we chose the parameterization $\tilde{\mathbf{z}} := (\bar{\mathbf{v}}, \mathbf{c}, \boldsymbol{\delta}, \bar{\mathbf{q}})$. In this new parameterization, constraint (3c) is replaced by

$$0.02 \cdot \mathbf{1} \leq \mathbf{c} \odot \bar{\mathbf{q}} \leq 0.18 \cdot \mathbf{1} - \boldsymbol{\delta} \quad (19)$$

which introduces bilinear terms too. Stability constraints (9) have already been transformed from $\boldsymbol{\alpha}$ to \mathbf{c} in (14).

Putting everything together, the bilevel ORD problem of (10) can be solved as the MINLP:

$$\tilde{\mathbf{z}}^* = \arg \min_{\tilde{\mathbf{z}}} \frac{1}{2S} \sum_{s=1}^S \|\mathbf{X} \mathbf{q}_s + \tilde{\mathbf{v}}_s - \mathbf{1}\|_2^2 \quad (20a)$$

$$\text{over } \tilde{\mathbf{z}} := (\bar{\mathbf{v}}, \mathbf{c}, \boldsymbol{\delta}, \bar{\mathbf{q}}) \quad (20b)$$

$$\text{s.to } (3a), (3b), (3d), (14), (19) \quad (20c)$$

$$(17a) - (17e) \quad \forall s \quad (20d)$$

$$(17f) - (17i) \text{ as in (18)} \quad \forall s. \quad (20e)$$

The bilinear terms in (17a) and (19), and the binary variables in (20e) increase with the number of inverters and scenarios.

Remark 1. The Volt/VAR curve of Fig. 1 has four degrees of freedom that control the center, deadband, slope, and saturation of the curve. These degrees of freedom are amenable to different equivalent parameterizations, such as $(\bar{\mathbf{v}}, \boldsymbol{\alpha}, \boldsymbol{\delta}, \boldsymbol{\sigma})$ and $(\bar{\mathbf{v}}, \mathbf{c}, \boldsymbol{\delta}, \boldsymbol{\sigma})$ that we used in Sec. IV; $(\bar{\mathbf{v}}, \boldsymbol{\alpha}, \boldsymbol{\delta}, \bar{\mathbf{q}})$; or $(\bar{\mathbf{v}}, \mathbf{c}, \boldsymbol{\delta}, \bar{\mathbf{q}})$. We used the last one in (20b) as it yielded significantly shorter solution times during our tests.

Although the MINLP approach can solve the ORD task to near-global optimality (modulo the bilinear terms left to be handled internally by the solver), it was found to scale unfavorably with the number of DERs and/or scenarios of Section VII.

VI. ORD FOR 3ϕ FEEDERS VIA DEEP LEARNING

Under transposed lines and balanced injections, one could deal with ORD using the single-phase formulations discussed earlier. Under imbalance conditions however, a linearized multiphase feeder model would be a better approximation. DERs would still implement local Volt/VAR rules, yet sensitivity matrix \mathbf{X} now has different properties as discussed in (1). For the multiphase case, we were not able to come up with an optimization problem whose minimizer coincides with the equilibrium setpoints \mathbf{q}^* similar to (6). Nonetheless, we show in the appendix that the Volt/VAR rules of Fig. 1 do converge to a unique equilibrium under the following polytopic conditions, which form a restriction of $\|\text{dg}(\boldsymbol{\alpha})\mathbf{X}\|_2 \leq 1 - \epsilon$.

Proposition 2. Consider the Volt/VAR dynamics of (5) operating over a multiphase feeder modeled by (1). If the Volt/VAR slope vector $\boldsymbol{\alpha}$ satisfies

$$|\mathbf{X}|^\top \boldsymbol{\alpha} \leq (1 - \epsilon) \cdot \mathbf{1} \quad (21a)$$

$$\alpha_n \leq \frac{1 - \epsilon}{\sum_{m \in \mathcal{N}} |X_{nm}|}, \quad \forall n \in \mathcal{N}. \quad (21b)$$

for $\epsilon \in (0, 1)$, the dynamics in (5) exhibit a unique equilibrium \mathbf{q}^* to which they converge exponentially fast as

$$\|\mathbf{q}^t - \mathbf{q}^*\|_2 \leq 2\|\hat{\mathbf{q}}\|_2 \cdot (1 - \epsilon)^t. \quad (21c)$$

The absolute value $|\mathbf{X}|$ applies entry-wise. The result generalizes (9) and [9, Th. 3] to multiphase feeders, wherein \mathbf{X} is non-symmetric and with some of its entries being negative. It provides linear constraints on $\boldsymbol{\alpha}$ to ensure stability.

The ORD task for multiphase feeders can be formulated as in (6) with the appropriate modification of the sensitivity matrix \mathbf{X} . Since equilibrium setpoints cannot be expressed as the minimizer of an inner optimization, the MINLP approach of Section V cannot be adopted here. Alternatively, one may pursue an MINLP formulation along the lines of [29], though scalability is still expected to be an issue. Fortunately, the DNN-based approach for ORD remains applicable with the next minor modifications: *i*) Sensitivity matrices are modified

accordingly; *ii*) Every layer now consists of $3N$ building modules corresponding to bus/phase (node) combinations; and *iii*) Use the stability constraints of (21) instead of (9).

Proposition 1 on minimum depth T of DNNs for Volt/VAR rules in single-phase feeders carries over to multiphase feeders. This is easily confirmed by applying the steps from the proof of Proposition 1 to the results from Proposition 2.

VII. NUMERICAL TESTS

The proposed ORD methods were evaluated on single- and multi-phase feeders. Real-world data of active load and solar generation at one-minute frequency was sourced from the Smart* project on April 2, 2011 [30]. The set consists of active loads from 444 homes and generation from 43 solar panels. Loads from multiple homes were averaged to better simulate loads at buses of the primary distribution network. Each averaged load was normalized so its peak value during the day coincided with the nominal active power load of its hosting node. For each time interval, reactive loads were added by randomly sampling lagging power factors within $[0.9, 1]$. Similarly to loads, each solar generation signal was normalized so its peak value was twice that of the nominal active load of the hosting bus. Apparent power limits for inverters were set to 1.1 times the peak active generation.

The control rules were designed and evaluated in Python on a 2.4 GHz 8-Core Intel Core i9 processor laptop computer with 64 GB RAM. Pytorch was selected as the library to design and train DNNs, as it implements computation graphs dynamically [28]. That is quite important for our purposes, as dynamic computation graphs imply that the number of layers T does not need to be fixed beforehand. It is rather decided on the fly based on the convergence of rules for the given $\tilde{\mathbf{v}}_t$. This flexibility enables limiting the DNN to lower depths. Convergence was determined based on the change in objective value with the addition of a layer. Specifically, the rules were assumed to have converged if the objective changed by less than $1 \cdot 10^{-7}$ within consecutive layers. All DNNs were trained using the Adam optimizer.

The projection step (15) was performed by solving a SOCP using the CVXPY library in Python with GUROBI as the solver. The MINLP (20) was implemented in MATLAB using YALMIP [31] with GUROBI, and used to benchmark the results for optimality and running time. Other specific details such as learning rates for DNN training, initialization of design parameters, load and solar panel assignments, and time period for scenario sampling are presented along with the corresponding results.

A. Tests on Single-Phase Feeder

The first set of tests was conducted on the single-phase equivalent of the IEEE 37-bus feeder. Homes with IDs 20–369 were averaged 10 at a time and successively added as active loads to buses 2–26 as shown in Fig. 6. Active generation from solar panels was also added, as per the mapping in Fig. 6. Additionally, buses {6, 9, 11, 12, 15, 16, 20, 22, 24, 25} were equipped with DERs capable of reactive power control.

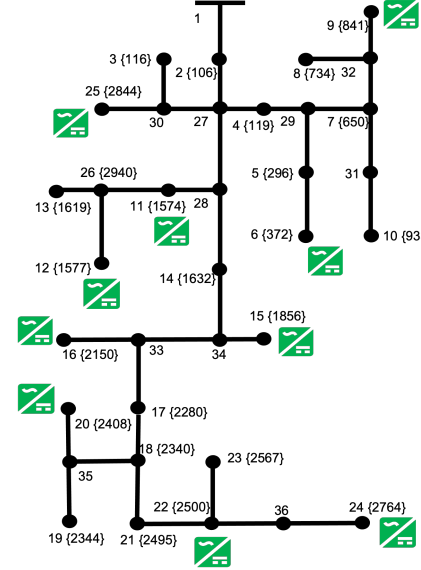


Fig. 6. The IEEE 37-bus feeder used for the tests. Node numbering follows the format node number {panel ID}. DERs at nodes {6, 9, 11, 12, 15, 16, 20, 22, 24, 25} provide reactive power control; the rest operate at unit power factor.

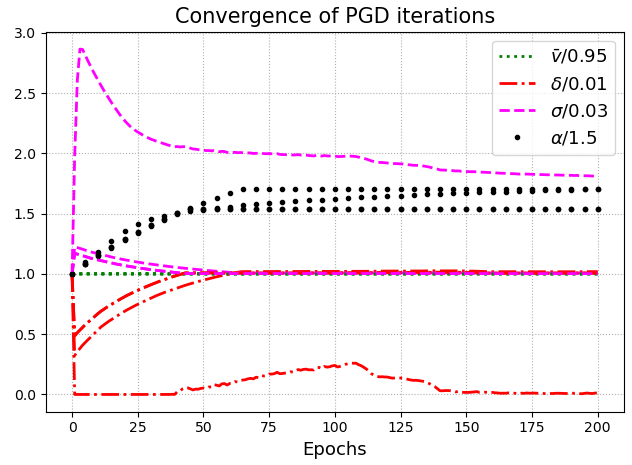


Fig. 7. Convergence of PGD iterations (12)–(15) for Volt/VAR rules with $\epsilon = 0.5$. Values of the rule parameters for DERs 12, 22, and 29 are plotted against training epochs. Plots have been normalized with respect to their initial values.

The DNN-based rules were optimized using 80 grid scenarios sampled from the high-solar period 3 : 00–3 : 20 pm, and were trained with the learning rate of 0.003 over 200 epochs. The design parameters $\mathbf{z} := (\bar{\mathbf{v}}, \delta, \sigma, \alpha)$ were initialized at the feasible point $(\bar{v}_n, \delta_n, \sigma_n, \alpha_n) = (0.95, 0.1, 0.3, 1.5)$ for all n . Figure 7 shows the convergence of Volt/VAR rule parameters for DERs at nodes {12, 22, 29}, for $\epsilon = 0.5$, during training. To accommodate different ranges of magnitudes, all plots are normalized with respect to their initial values.

Figure 8 highlights the efficacy of the optimized Volt/VAR rules in improving the voltage profile across the feeder. Voltages across buses are plotted under three setups: voltages without DER reactive power support, voltages under the default settings $(\bar{v}_n, \delta_n, \sigma, \bar{q}_n) = (1, 0.02, 0.08, \hat{q}_n)$ from IEEE

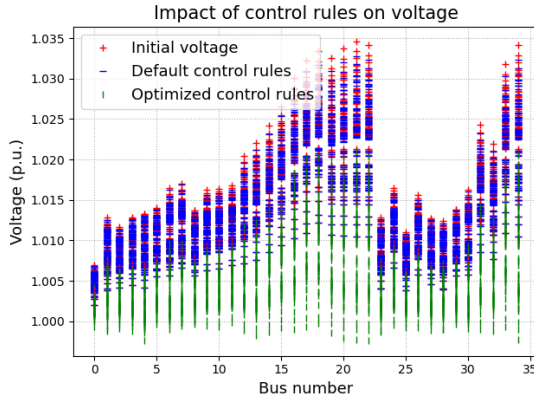


Fig. 8. Voltages across the buses of the IEEE 37-bus feeder for 80 scenarios. Voltages are highest without reactive power compensation. While the control rules with the default settings only marginally lower voltages closer to 1, they are significantly outmatched by control rules with optimal design parameters.

TABLE I
TEST RESULTS CAPTURING THE EFFECT OF ϵ ON THE OPTIMAL OBJECTIVE VALUE FOR VOLT/VAR CONTROL RULES. THE SMALLER THE ϵ , THE LARGER THE FEASIBLE REGION FOR RULE PARAMETERS IS, AND SO LOWER VOLTAGE REGULATION VALUES CAN BE ATTAINED.

ϵ	α_{init}	Objective (p.u.)
0.9	0.4	$2.22 \cdot 10^{-3}$
0.8	0.5	$1.37 \cdot 10^{-3}$
0.7	1	$1.06 \cdot 10^{-3}$
0.6	1.5	$9.73 \cdot 10^{-4}$
0.5	1.5	$8.50 \cdot 10^{-4}$

1547.8 [4]; and voltages under control rules with optimal \mathbf{z} . For each bus, voltages for all $S = 80$ scenarios have been marked. The default control rules were found to only marginally improve voltage profiles. On the other hand, optimally designed control rules were successful in significantly lowering voltages and bringing them close to unity at all buses.

We next studied the impact of the stability margin ϵ on the optimal cost $L(\mathbf{z})$ of (11) under Volt/VAR rules. Recall that ϵ determines the feasible space of design parameters via (9). The larger the ϵ , the more restricted problem (10) is. Table I confirms this by presenting the objectives during training for a range of ϵ values. Table I also lists the chosen initial value for α , represent by α_{init} , that renders the initial \mathbf{z} feasible for the corresponding value of ϵ . The objective converged to the highest value for $\epsilon = 0.9$ and the lowest for $\epsilon = 0.5$. Note that for the studied scenarios, reducing ϵ below 0.5 did not impact the optimal value of the objective, which indicates that the feasible space for $\epsilon = 0.5$ contains the optimizers for all $\epsilon \leq 0.5$ as well. Consequently, the value of ϵ has been fixed at 0.5 for the subsequent results on the 37-bus feeder.

To verify the optimality and scalability of DNN-based ORD, we benchmarked them against the MINLP formulation of (20). The MINLP was allowed to run until completion or till 300 seconds, whichever happened earlier. Scaling with respect to both the number of scenarios as well as DERs was studied. Table II reports the results for the case when the number of smart DERs was fixed to $N_G = 5$ and scenarios were increased from $S = 10$ to 80. As evident from Table II, the DNN-

TABLE II
TESTS COMPARING THE MINLP WITH THE DNN-BASED ORD FOR DIFFERENT NUMBERS OF SCENARIOS S , WITH $N_G = 5$ SMART DERs.

S	MINLP			DNN	
	Solved	Time (s)	Obj. (p.u.)	Time (s)	Obj. (p.u.)
10	Yes	2.45	$9.82 \cdot 10^{-4}$	18.16	$9.82 \cdot 10^{-4}$
20	Yes	3.64	$1.57 \cdot 10^{-3}$	20.08	$1.58 \cdot 10^{-3}$
40	Yes	123.32	$2.78 \cdot 10^{-3}$	20.63	$2.78 \cdot 10^{-3}$
80	No	300	$2.68 \cdot 10^{-3}$	22.17	$2.62 \cdot 10^{-3}$

TABLE III
COMPARING MINLP WITH THE DNN-BASED APPROACH FOR DIFFERENT N_G AND $S = 80$.

N_G	MINLP			DNN	
	Solved	Time (s)	Obj. (p.u.)	Time (s)	Obj. (p.u.)
2	Yes	3.90	$3.62 \cdot 10^{-3}$	14.12	$3.62 \cdot 10^{-3}$
4	No	300	$3.22 \cdot 10^{-3}$	17.96	$3.18 \cdot 10^{-3}$
6	No	300	$2.77 \cdot 10^{-3}$	21.95	$2.35 \cdot 10^{-3}$
8	No	300	$1.40 \cdot 10^{-3}$	33.42	$1.16 \cdot 10^{-3}$
10	No	300	$1.20 \cdot 10^{-3}$	39.76	$8.50 \cdot 10^{-4}$

based ORD scaled much better than the MINLP for larger S , as expected. Furthermore, the DNN-based ORD was able to achieve the same objective as the MINLP across all tested values of S , which is remarkable since SGD for non-convex problems can only guarantee convergence to stationary points. Similar conclusions can be drawn from Table III where we fixed $S = 80$ and varied N_G from 2 to 10. The MINLP was faster than the DNN-based approach for $N_G = 2$, but could not be solved within 300 seconds if more inverters were added. On the other hand, the DNN-based ORD scaled gracefully with the N_G and achieved lower objectives for all $N_G \geq 4$.

The scalability of the DNN-based control rules was also confirmed by implementing them for the larger IEEE 123-bus feeder of Fig. 9. Active load data was generated by averaging homes with IDs 20-386, three at a time, and were serially assigned them to buses 2-123. Solar generation from 10 panels with IDs {106, 116, 119, 296, 372, 650, 734, 841, 933, 1574} was added to buses {17, 29, 32, 39, 50, 71, 78, 96, 100, 114}, respectively. All buses with solar were equipped with smart DERs for reactive power support. The DNNs for Volt/VAR rules were trained with the learning rate of 0.01, with ϵ set to 0.5. The design parameters $\mathbf{z} := (\bar{\mathbf{v}}, \delta, \sigma, \alpha)$ were initialized at the feasible point $(1.05, 0.1, 0.3, 1.5)$. With N_G and S fixed at 10 and 80, respectively, the DNN-based ORD was compared to the MINLP one. For this larger network, the MINLP solver was allowed to run until 500 seconds. To ensure repeatability, the results were repeated across several time periods between 1 – 6 PM, and have been compiled in Table IV. For all time periods, the DNN-based solver scaled well in terms of the DNN training time. The MINLP solver could not converge within 500 seconds and was outperformed by the DNN-based solver in terms of final objective values across all setups.

B. Tests on a Multiphase Feeder

The DNN-based control rules were also tested on the multiphase IEEE 13-bus feeder. Active loads from homes with IDs 20-379 were averaged ten homes at a time. The resulting 36 averaged loads were added to buses 1-12, allocating all three phases for a bus before moving on to the next one. Solar

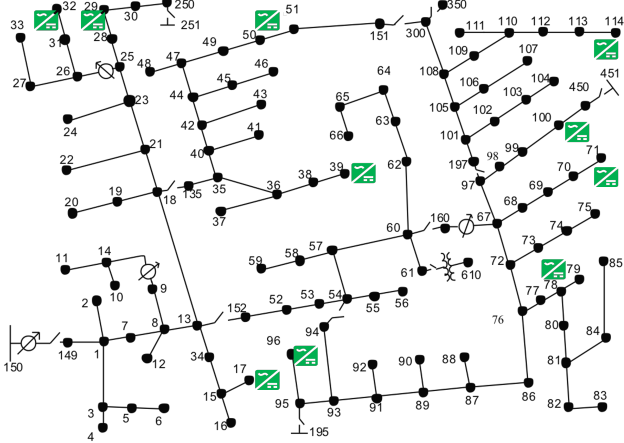


Fig. 9. Inverter siting on the IEEE 123-bus distribution feeder.

TABLE IV
TEST RESULTS COMPARING THE MINLP WITH THE DNN-BASED ORD APPROACH FOR THE SINGLE-PHASE IEEE 123-BUS FEEDER, ACROSS DIFFERENT TIME PERIODS FOR $N_G = 10$ DERs AND $S = 80$ SCENARIOS.

Time	MINLP			DNN	
	Solved	Time (s)	Obj. (p.u.)	Time (s)	Obj. (p.u.)
1 pm	No	500	$9.26 \cdot 10^{-4}$	28.6	$8.95 \cdot 10^{-4}$
2 pm	No	500	$6.69 \cdot 10^{-4}$	30.18	$6.40 \cdot 10^{-4}$
3 pm	No	500	$4.17 \cdot 10^{-4}$	27.55	$3.92 \cdot 10^{-4}$
4 pm	No	500	$2.17 \cdot 10^{-4}$	29.83	$2.09 \cdot 10^{-4}$
5 pm	No	500	$2.98 \cdot 10^{-3}$	27.53	$2.87 \cdot 10^{-4}$

generation was added to nodes as per the panel assignments shown in Fig. 10. Values in red, green, and blue correspond to panel IDs assigned to Phases A, B, and C, respectively. Reactive power compensation was provided by nine inverters added across phases, and bus indices, as shown in Fig 10, with the colors indicating the corresponding phase.

The learning rate for DNN-based control rules was set to 0.1, with the design parameters $\mathbf{z} := (\bar{\mathbf{v}}, \delta, \sigma, \alpha)$ initialized to feasible values $(0.95, 0.01, 0.3, 1.5)$. In the absence of an MINLP solver, the optimized DNN-based control rules were benchmarked against control rules with the default settings from the IEEE 1547.8 standard. Table V collects the values for the objective (10) for $S = 80$ scenarios, across different windows of time from 1–5 pm, under three control schemes—no reactive power compensation, optimized control rules, and default control rules. The default control rules did not manage to significantly reduce the objective (10), as the grid conditions $\bar{\mathbf{v}}$ were observed to frequently fall in the deadband of the default control rules. In contrast, the optimized control rules took the grid conditions $\bar{\mathbf{v}}$ into consideration while designing the deadband, and hence improved voltage profiles considerably.

VIII. CONCLUSIONS

This work has genuinely reformulated the ORD problem to the task of training a DNN using grid scenarios as training data, unit voltages as desired targets for equilibrium voltages, and Volt/VAR rule parameters as weights. The proposed DNN-based ORD framework is general enough to accommodate Volt/VAR rules on single- and multi-phase feeders. We have

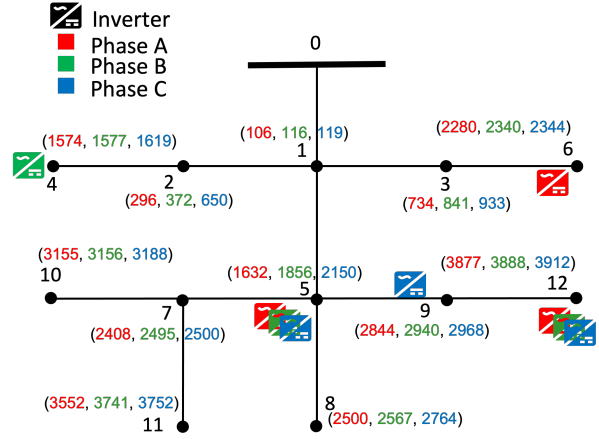


Fig. 10. The three-phase IEEE 13-bus distribution feeder system.

TABLE V
TEST RESULTS ON THE MULTIPHASE IEEE 13-BUS FEEDER FOR $N_G = 9$ INVERTERS AND $S = 80$ SCENARIOS. COMPARING THE OBJECTIVE (10) UNDER THREE SCENARIOS: NO REACTIVE POWER COMPENSATION, OPTIMIZED CONTROL RULES, AND THE DEFAULT RULES PER IEEE 1547.

Time	$\mathbf{q} = 0$	Optimized	Default
1 pm	$2.51 \cdot 10^{-3}$	$1.15 \cdot 10^{-3}$	$2.31 \cdot 10^{-3}$
2 pm	$1.48 \cdot 10^{-3}$	$6.89 \cdot 10^{-4}$	$1.42 \cdot 10^{-4}$
3 pm	$6.89 \cdot 10^{-4}$	$4.94 \cdot 10^{-4}$	$6.89 \cdot 10^{-4}$
4 pm	$8.03 \cdot 10^{-4}$	$5.26 \cdot 10^{-4}$	$8.03 \cdot 10^{-4}$
5 pm	$5.51 \cdot 10^{-4}$	$4.11 \cdot 10^{-4}$	$5.51 \cdot 10^{-4}$

also reviewed and extended results on the stability and convergence rates of Volt/VAR control rules. For benchmarking purposes, we have also developed an MINLP approach to ORD. The suggested approaches have been validated using real-world data on IEEE test feeders. The tests show that DNN-based ORD seems to outperform the MINLP approach in terms of optimality under time budgets and that optimized ORD curves outperform the default values. Our findings form the foundations for exciting research directions, such as: *d1*) Can the DNN-based ORD framework be extended to designing *incremental* Volt/VAR control rules with favorable stability characteristics? *d2*) What are the appropriate Volt/VAR control rules for three-phase (probably large-scale utility-owned) DERs? *d3*) How can ORD be jointly performed with topology reconfiguration or with optimally setting regulator and capacitor settings? *d4*) Could other voltage regulation or OPF formulations be combined with the DNN-based methodology? *d5*) Can more detailed grid models be incorporated in ORD?

APPENDIX

Proof of Proposition 1: By a contraction mapping argument, reference [9] proves that as long as stable, the Volt/VAR dynamics \mathbf{q}^t enjoy exponential convergence to the equilibrium \mathbf{q}^* . That means that if $\| \mathbf{d}\mathbf{g}(\alpha) \mathbf{X} \|_2 < 1$, then

$$\| \mathbf{q}^t - \mathbf{q}^* \|_2 \leq \| \mathbf{d}\mathbf{g}(\alpha) \mathbf{X} \|_2 \cdot \| \mathbf{q}^{t-1} - \mathbf{q}^* \|_2.$$

Propagating the previous claim across time and for ϵ -stable rules $\| \mathbf{d}\mathbf{g}(\alpha) \mathbf{X} \|_2 \leq 1 - \epsilon$, we get that

$$\| \mathbf{q}^t - \mathbf{q}^* \|_2 \leq \| \mathbf{q}^0 - \mathbf{q}^* \|_2 \cdot (1 - \epsilon)^t \leq 2 \| \hat{\mathbf{q}} \|_2 \cdot (1 - \epsilon)^t$$

since the initial distance to the equilibrium can be upper bounded by $\|\mathbf{q}^0 - \mathbf{q}^*\|_2 \leq 2\|\hat{\mathbf{q}}\|_2$. Because $\mathbf{v} = \mathbf{X}\mathbf{q} + \tilde{\mathbf{v}}$, translate injection distances to voltage distances

$$\|\mathbf{v}^t - \mathbf{v}^*\|_2 \leq 2\|\mathbf{X}\|_2\|\hat{\mathbf{q}}\|_2(1-\epsilon)^t.$$

To ensure the voltage approximation error at time T is smaller than ϵ_1 , or $\|\mathbf{v}^T - \mathbf{v}^*\|_2 \leq 2\|\mathbf{X}\|_2\|\hat{\mathbf{q}}\|_2(1-\epsilon)^T \leq \epsilon_1$, it suffices to select T as

$$T \log(1-\epsilon) \leq \log \frac{\epsilon_1}{2\|\mathbf{X}\|_2\|\hat{\mathbf{q}}\|_2}.$$

The claim follows by noticing that $\log(1-\epsilon) < 0$. \square

Proof of Proposition 2: Reference [9, Th. 3] shows that the Volt/VAR rules of $\mathbf{f}(\cdot)$ are Lipschitz continuous in \mathbf{q} with $\|\mathbf{dg}(\alpha)\mathbf{X}\|_2$ as the Lipschitz constant, that is

$$\|\mathbf{f}(\mathbf{q}) - \mathbf{f}(\mathbf{q}')\|_2 \leq \|\mathbf{dg}(\alpha)\mathbf{X}\|_2 \cdot \|\mathbf{q} - \mathbf{q}'\|_2 \quad (22)$$

for any \mathbf{q} and \mathbf{q}' obeying (3d). From Hölder's inequality for matrix norms, it holds that

$$\begin{aligned} \|\mathbf{dg}(\alpha)\mathbf{X}\|_2^2 &\leq \|\mathbf{dg}(\alpha)\mathbf{X}\|_1 \cdot \|\mathbf{dg}(\alpha)\mathbf{X}\|_\infty \\ &= \|\mathbf{dg}(\alpha)|\mathbf{X}|\|_1 \cdot \|\mathbf{dg}(\alpha)|\mathbf{X}|\|_\infty \end{aligned}$$

where $\|\cdot\|_1$ and $\|\cdot\|_\infty$ are defined as the maximum absolute sums column-wise and row-wise, respectively. The equality holds because α has positive entries. It is easy to check that $\|\mathbf{dg}(\alpha)|\mathbf{X}|\|_1$ is the maximum entry of vector $|\mathbf{X}|^\top \alpha$, and $\|\mathbf{dg}(\alpha)|\mathbf{X}|\|_\infty$ is the maximum entry of vector $\mathbf{dg}(|\mathbf{X}|1)\alpha$. Consequently, enforcing (21) results in $\|\mathbf{dg}(\alpha)\mathbf{X}\|_2 \leq (1-\epsilon)$. Substituting $\|\mathbf{dg}(\alpha)\mathbf{X}\|_2 < (1-\epsilon)$ in (22) yields

$$\|\mathbf{f}(\mathbf{q}) - \mathbf{f}(\mathbf{q}')\|_2 \leq (1-\epsilon)\|\mathbf{q} - \mathbf{q}'\|_2 \quad (23)$$

Since $\epsilon \in (0, 1)$, the above relation is a contraction mapping over the space $\mathbf{q} \in [-\bar{\mathbf{q}}, \bar{\mathbf{q}}]$ with respect to the ℓ_2 -norm. The latter establishes the existence and uniqueness of the equilibrium, as well as the exponential convergence of Volt/VAR dynamics. To explicitly derive the convergence result (21c), note that $\mathbf{q}^t = \mathbf{f}(\mathbf{q}^{t-1})$ and $\mathbf{q}^* = \mathbf{f}(\mathbf{q}^*)$. From (23), we get

$$\|\mathbf{q}^t - \mathbf{q}^*\|_2 \leq (1-\epsilon)\|\mathbf{q}^{t-1} - \mathbf{q}^*\|_2 \leq (1-\epsilon)^t\|\mathbf{q}^0 - \mathbf{q}^*\|_2.$$

The claim follows as $\|\mathbf{q}^0 - \mathbf{q}^*\|_2 \leq 2\|\hat{\mathbf{q}}\|_2$. \square

REFERENCES

- [1] M. Farivar, R. Neal, C. Clarke, and S. Low, "Optimal inverter VAR control in distribution systems with high PV penetration," in *Proc. IEEE Power & Energy Society General Meeting*, San Diego, CA, Jul. 2012.
- [2] Y. Zhang, N. Gatsis, and G. B. Giannakis, "Robust energy management for microgrids with high-penetration renewables," *IEEE Trans. Sustain. Energy*, vol. 4, no. 4, pp. 944–953, Oct. 2013.
- [3] F. Mancilla-David, A. Angulo, and A. Street, "Power management in active distribution systems penetrated by photovoltaic inverters: A data-driven robust approach," *IEEE Trans. Smart Grid*, vol. 11, no. 3, pp. 2271–2280, May 2020.
- [4] *IEEE Standard for Interconnection and Interoperability of Distributed Energy Resources with Associated Electric Power Systems Interfaces*, IEEE Std., 2018.
- [5] G. Cavraro, S. Bolognani, R. Carli, and S. Zampieri, "The value of communication in the voltage regulation problem," in *Proc. IEEE Conf. on Decision and Control*, 2016, pp. 5781–5786.
- [6] S. Magnússon, G. Qu, C. Fischer, and N. Li, "Voltage control using limited communication," *IEEE Trans. Control of Network Systems*, vol. 6, no. 3, pp. 993–1003, Sep. 2019.
- [7] M. Farivar, L. Chen, and S. Low, "Equilibrium and dynamics of local voltage control in distribution systems," in *52nd IEEE Conference on Decision and Control*, Dec 2013, pp. 4329–4334.
- [8] X. Zhou, J. Tian, L. Chen, and E. Dall'Anese, "Local voltage control in distribution networks: A game-theoretic perspective," in *2016 North American Power Symposium (NAPS)*, Nov 2016, pp. 1–6.
- [9] X. Zhou, M. Farivar, Z. Liu, L. Chen, and S. H. Low, "Reverse and forward engineering of local voltage control in distribution networks," *IEEE Trans. Autom. Contr.*, vol. 66, no. 3, pp. 1116–1128, 2021.
- [10] V. Calderaro, G. Conio, V. Galdi, G. Massa, and A. Piccolo, "Optimal decentralized voltage control for distribution systems with inverter-based distributed generators," *IEEE Trans. Power Syst.*, vol. 29, no. 1, pp. 230–241, Jan. 2014.
- [11] A. Samadi, R. Eriksson, L. Söder, B. G. Rawn, and J. C. Boemer, "Coordinated active power-dependent voltage regulation in distribution grids with PV systems," *IEEE Trans. Power Del.*, vol. 29, no. 3, pp. 1454–1464, Jun 2014.
- [12] A. Singhal, V. Ajjarapu, J. Fuller, and J. Hansen, "Real-time local Volt/Var control under external disturbances with high PV penetration," *IEEE Trans. Smart Grid*, vol. 10, no. 4, pp. 3849–3859, Jul. 2019.
- [13] R. A. Jabr, "Segregated linear decision rules for inverter Watt-Var control," *IEEE Trans. Power Syst.*, vol. 36, no. 3, pp. 2702–2708, 2021.
- [14] K. Baker, A. Bernstein, E. Dall'Anese, and C. Zhao, "Network-cognizant voltage droop control for distribution grids," *IEEE Transactions on Power Systems*, vol. 33, no. 2, pp. 2098–2108, 2018.
- [15] J. Sepulveda, A. Angulo, F. Mancilla-David, and A. Street, "Robust co-optimization of droop and affine policy parameters in active distribution systems with high penetration of photovoltaic generation," *IEEE Trans. Smart Grid*, pp. 1–1, 2022.
- [16] I. Murzakhanov, S. Gupta, S. Chatzivasileiadis, and V. Kekatos, "Optimal design of Volt/VAR control rules for inverter-interfaced distributed energy resources," *IEEE Trans. Smart Grid*, 2023, (submitted). [Online]. Available: <https://arxiv.org/abs/2210.12805>
- [17] W. Wang, N. Yu, Y. Gao, and J. Shi, "Safe off-policy deep reinforcement learning algorithm for Volt-Var control in power distribution systems," *IEEE Trans. Smart Grid*, vol. 11, no. 4, pp. 3008–3018, Jul. 2020.
- [18] Q. Zhang, K. Dehghanpour, Z. Wang, F. Qiu, and D. Zhao, "Multi-agent safe policy learning for power management of networked microgrids," *IEEE Trans. Smart Grid*, vol. 12, no. 2, pp. 1048–1062, Mar. 2021.
- [19] S. Gupta, V. Kekatos, and M. Jin, "Controlling smart inverters using proxies: A chance-constrained DNN-based approach," *IEEE Trans. Smart Grid*, vol. 13, no. 2, pp. 1310–1321, Mar. 2022.
- [20] M. K. Singh, S. Gupta, V. Kekatos, G. Cavraro, and A. Bernstein, "Learning to optimize power distribution grids using sensitivity-informed deep neural networks," in *Proc. IEEE Intl. Conf. on Smart Grid Commun.*, Tempe, AZ, Nov. 2020, pp. 1–6.
- [21] M. Jalali, V. Kekatos, N. Gatsis, and D. Deka, "Designing reactive power control rules for smart inverters using support vector machines," *IEEE Trans. Smart Grid*, vol. 11, no. 2, pp. 1759–1770, Mar. 2020.
- [22] M. Jalali, M. K. Singh, V. Kekatos, G. B. Giannakis, and C. C. Liu, "Fast inverter control by learning the OPF mapping using sensitivity-informed Gaussian processes," *IEEE Trans. Smart Grid*, 2022, (early access).
- [23] W. Cui, J. Li, and B. Zhang, "Decentralized safe reinforcement learning for inverter-based voltage control," *Electric Power Systems Research*, vol. 211, p. 108609, 2022.
- [24] S. Taheri, M. Jalali, V. Kekatos, and L. Tong, "Fast probabilistic hosting capacity analysis for active distribution systems," *IEEE Trans. Smart Grid*, vol. 12, no. 3, pp. 2000–2012, May 2021.
- [25] M. Baran and F. Wu, "Optimal sizing of capacitors placed on a radial distribution system," *IEEE Trans. Power Syst.*, vol. 4, no. 1, pp. 735–743, Jan. 1989.
- [26] M. Farivar, L. Chen, and S. Low, "Equilibrium and dynamics of local voltage control in distribution systems," in *Proc. IEEE Conf. on Decision and Control*, Florence, Italy, Dec. 2013, pp. 4329–4334.
- [27] V. Kekatos, L. Zhang, G. B. Giannakis, and R. Baldick, "Voltage regulation algorithms for multiphase power distribution grids," *IEEE Trans. Power Syst.*, vol. 31, no. 5, pp. 3913–3923, Sep. 2016.
- [28] Pytorch. [Online]. Available: <https://pytorch.org/blog/computational-graphs-constructed-in-pytorch/>
- [29] M. K. Singh, S. Taheri, V. Kekatos, K. P. Schneider, and C.-C. Liu, "Joint grid topology reconfiguration and design of Watt-VAR curves for DERs," in *Proc. IEEE Power & Energy Society General Meeting*, Denver, CO, Jul. 2022.
- [30] D. Chen, S. Iyengar, D. Irwin, and P. Shenoy, "Sunspot: Exposing the location of anonymous solar-powered homes," in *ACM Intl. Conf. on Systems for Energy-Efficient Built Environments*, Palo Alto, CA, Nov. 2016, p. 85–94.
- [31] J. Lofberg, "A toolbox for modeling and optimization in MATLAB," in *Proc. of the CACSD Conf.*, 2004.